

ARTICLE

Open Access

# Tailored lead iodide growth for efficient flexible perovskite solar cells and thin-film tandem devices

Stefano Pisoni<sup>1</sup>, Romain Carron<sup>1</sup>, Thierry Moser<sup>1</sup>, Thomas Feurer<sup>1</sup>, Fan Fu<sup>1,2</sup>, Shiro Nishiwaki<sup>1</sup>, Ayodhya N. Tiwari<sup>1</sup> and Stephan Buecheler<sup>1</sup>

## Abstract

Flexible perovskite solar cells (PSCs) hold great promise for the low-cost roll-to-roll production of lightweight single- and multijunction photovoltaic devices. Among the different deposition methods used for the perovskite absorber, the two-step hybrid vacuum-solution approach enables precise control over the thickness and morphology of  $\text{PbI}_2$ . However, efficient conversion to perovskite is limited by diffusion of the organic cations in the compact lead halide layer. Herein, a multistage absorber deposition is developed by thermal evaporation of  $\text{PbI}_2$  and spin coating of  $\text{CH}_3\text{NH}_3\text{I}$  (MAI). The process relies on the different types of growth of vacuum-deposited  $\text{PbI}_2$  onto amorphous and crystalline surfaces. This approach represents a way to effectively increase the absorber thickness while tackling the limited MAI diffusion in the compact  $\text{PbI}_2$  film via a two-step deposition method. The efficiency of flexible PSCs is improved from 14.2 to 15.8% with multistage deposition. Furthermore, the use of an amorphous transparent conductive oxide (TCO),  $\text{InZnO}$ , enhances the mechanical resistance against bending with respect to conventional crystalline TCO-based flexible devices. Near-infrared transparent flexible PSCs are developed with an efficiency of 14.0% and average transmittance of ~74% between 800 and 1000 nm. Flexible perovskite/CIGS thin-film tandem devices are demonstrated with an efficiency of 19.6% measured in the four-terminal configuration.

## Introduction

Solar cells developed on lightweight flexible substrates represent an interesting option for future energy generation applications. The possibility to produce flexible photovoltaic devices by high throughput roll-to-roll manufacturing opens up the way towards cost reduction compared to traditional sheet-to-sheet processes. Recently, hybrid organic-inorganic perovskites have emerged as a new generation of low-cost photovoltaic materials. The high absorption coefficient, high bandgap (~1.6 eV) and low Urbach energy make perovskites ideal

absorbers for single- and multijunction devices<sup>1,2</sup>. Among different perovskite-based multijunction technologies<sup>3,4</sup>, all-thin-film perovskite/ $\text{Cu}(\text{In},\text{Ga})\text{Se}_2$  (CIGS) tandem devices have shown an outstanding performance improvement in the last three years, reaching efficiencies as high as 23.9%<sup>5</sup>. It has to be noted that the top and bottom cells in these tandem devices are grown onto rigid glass substrates. The demonstration of highly efficient flexible perovskite and CIGS solar cells<sup>6,7</sup> has laid the foundations for flexible thin-film tandem devices<sup>8</sup> with the promise of future roll-to-roll manufacturing of lightweight perovskite-based multijunction devices.

An interesting feature of perovskite solar cells (PSCs) is the wide versatility afforded by low-temperature deposition processes<sup>9–11</sup>. Among different deposition techniques, the hybrid vacuum-solution two-step method holds great potential for control of the  $\text{PbI}_2$  thickness and

Correspondence: Stefano Pisoni ([stefano.pisoni@empa.ch](mailto:stefano.pisoni@empa.ch))

<sup>1</sup>Laboratory for Thin Films and Photovoltaics, Empa-Swiss Federal Laboratories for Materials Science and Technology, Ueberlandstrasse 129, 8600 Dübendorf, Switzerland

<sup>2</sup>now at Photovoltaics and Thin-Film Electronics Laboratory (PV-Lab), Ecole Polytechnique Fédérale de Lausanne (EPFL), Rue de la Maladière 71b, 2002 Neuchâtel, Switzerland

morphology to obtain compact and pinhole-free absorber layers<sup>12</sup>. Traditional solution-based processes, such as one- or two-step deposition, rely on the use of dimethylformamide (DMF) and dimethyl sulfoxide (DMSO)<sup>13</sup>. These solvents are not suitable with low-temperature deposited efficient organic-based electron transport layer (ETL) such as C<sub>60</sub><sup>14</sup>. On the other hand, thermal evaporation of PbI<sub>2</sub> followed by CH<sub>3</sub>NH<sub>3</sub>I (MAI) spin coating from isopropanol solution does not damage the very thin organic charge extraction layer. In a two-step deposition, the conversion to high-quality perovskite absorbers is dictated by the diffusion and intercalation of the organic cations into the inorganic PbI<sub>2</sub> layered structure. Once the organic cation is deposited, the intercalation starts at the edge-air interface, where organic moieties immediately form hydrogen bonds with the inorganic sites. The thin surface layer of CH<sub>3</sub>NH<sub>3</sub>PbI<sub>3</sub>, which is suddenly formed, hinders further diffusion of MAI cations to the inner lead sites due to lack of Van der Waals gaps in the perovskite structure<sup>15,16</sup>. For this reason, a finely tailored PbI<sub>2</sub> morphology is needed to facilitate MAI cation diffusion and play a fundamental role in the conversion to the perovskite absorber.

Different approaches have been reported to effectively engineer the PbI<sub>2</sub> morphology, facilitating organic cation intercalation. Wu et al.<sup>17</sup> showed the possibility to retard PbI<sub>2</sub> compact-layer crystallization by coordination with DMSO molecules, improving the conversion to the perovskite phase. Tu et al.<sup>18</sup> demonstrated solvent substitution to finely control the PbI<sub>2</sub> nuclei growth and recrystallization process. Zhang et al.<sup>19</sup> reported improved organic cation intercalation and conversion reaction by pre-expansion of the PbI<sub>2</sub> layer using a mixed PbI<sub>2</sub>:MAI precursor. Even if these approaches offer suitable solutions to significantly improve device efficiency, they cannot be applied when PbI<sub>2</sub> is grown by vacuum deposition methods.

As we observed, in a hybrid two-step vacuum-solution process, the growth of thermally evaporated PbI<sub>2</sub> depends on the substrate surface<sup>20</sup>. A compact morphology is observed once PbI<sub>2</sub> is thermally evaporated onto amorphous surfaces due to a preferential growth parallel to the substrate as a result of minimization of combined surface and interface energy. On the other hand, a nanoplate-like morphology is formed onto crystalline substrates due to both the anisotropic nature of the substrate and interface energy<sup>20</sup>.

Here we report a modified two-step hybrid vacuum-solution deposition method to effectively increase the absorber thickness. The morphology of PbI<sub>2</sub> is tailored by a multistage deposition, where the first stage is characterized by a compact inorganic layer, and the second stage, by a nanoplate-like morphology. By careful screening of the organic cation concentration and

nanoplate-like lead iodide thickness, we are able to demonstrate flexible PSC with a steady-state efficiency of 15.8% compared to a 14.2% efficient device prepared by a traditional two-step hybrid process.

For the transparent conductive oxide (TCO), we use sputtered InZnO (IZO), which displays high near-infrared transparency and an amorphous nature. The latter characteristic enables one to obtain highly flexible PSCs with respect to conventional flexible PSCs based on crystalline TCO. The devices retain 90 and 80% of the original efficiency after 1000 bending cycles at bending radii of 6 and 4 mm, respectively. Furthermore, the high near-infrared transparency of the TCO makes it suitable for use in tandem applications. We are able to demonstrate a NIR-transparent flexible PSC with a steady state efficiency of 14.0% and average transmittance of ~74% between 800 and 1000 nm. By combining the flexible perovskite top cell with a flexible CIGS bottom cell, we demonstrate an efficiency of 19.6% measured in the four-terminal tandem configuration. Eventually, we present optical loss analysis to establish future steps towards realization of higher-efficiency flexible perovskite/CIGS tandem devices.

## Materials and methods

### Materials

An InZnO target was bought from JX Nippon Mining & Metals (99.9%). Spiro-OMeTAD was bought from Merck. Polyethylenimine, 80% ethoxylated solution, 35-40 wt.% in H<sub>2</sub>O, 4-tertbutylpyridine (TBP) were bought from Sigma-Aldrich. CH<sub>3</sub>NH<sub>3</sub>I (powder, ITEM# MS101000) and PbI<sub>2</sub> (ultradry, 99.999%, metals basis) were purchased from Dyesol (Australia) and Alfa Aesar, respectively. Fullerene carbon 60 powder (C<sub>60</sub>) was bought from SES Research (purity > 99.5%). All chemicals were used as received without any further treatment or purification.

### Photovoltaic device fabrication

PSCs are grown onto a flexible foil, which is used as moisture barrier front sheet for encapsulation in flexible CIGS modules. Then, 5 × 5 cm size flexible substrates are washed by hand followed by ultrasonic soap and water baths. The substrates are dried in vacuum for one week and cut into 4 quarters (2.5 × 2.5 cm). Prior to further processing, ~200 nm of compact InZnO (IZO) layer is deposited at room temperature by pulsed-DC sputtering from a ceramic In<sub>0.89</sub>Zn<sub>0.11</sub>O target, at 600 W. The sheet resistance of the as-deposited film on glass is measured to be 18 Ω□ by a four-probe method. Then, the IZO layer is treated for 10 min under UV light for all the samples. PEIE interlayer (0.1% w/w) in deionized (DI) water is deposited onto the IZO layer by spin coating (5000 r.p.m., 5000 rpm s<sup>-1</sup> for 60 s) followed by annealing at 100 °C for 10 min. Then, ~5 nm of C<sub>60</sub> is thermally evaporated in a N<sub>2</sub> filled glovebox. The PbI<sub>2</sub> film is thermally evaporated at a deposition

pressure of  $2\text{--}6 \times 10^{-6}$  Pa. The deposition rate is controlled within  $1.2\text{--}1.6 \text{ \AA s}^{-1}$ , monitored by a quartz crystal microbalance. The thickness of  $\text{PbI}_2$  is 140 nm. After the  $\text{PbI}_2$  deposition, the samples are subsequently transferred into a  $\text{N}_2$ -filled glove-box for further processing. The perovskite layer is formed by spin coating of  $\text{CH}_3\text{NH}_3\text{I}$  in 2-propanol at a concentration of 55 mg mL $^{-1}$ . The solution is first spread to cover the whole substrate followed by waiting for 5 s before starting the rotation (4000 rpm, 4000 rpm s $^{-1}$  for 40 s). The as-prepared films are annealed at 100 °C for 30 min on a hotplate inside the glovebox. In the case of multistage deposition, after perovskite annealing, a  $\text{PbI}_2$  film is thermally evaporated for the second time, following the same conditions used for the first stage. Different thicknesses have been investigated (80, 100, 120 and 140 nm). Then,  $\text{CH}_3\text{NH}_3\text{I}$  in 2-propanol is spin-coated at different concentrations for every  $\text{PbI}_2$  thickness, as reported in the *Results and discussion* section. The as-prepared films are annealed at 100 °C for 30 min on a hotplate inside the glovebox. After annealing, the samples are cooled down to room temperature, and 100  $\mu\text{L}$  of a Spiro-OMeTAD solution (78.2 mg 2,2',7,7'-tetrakis-(N,N'-di-*p*-methoxyphenylamine)-9,9'-spirobi-fluorene (Spiro-OMeTAD), 33  $\mu\text{L}$  of a lithium-bis(trifluoromethanesulfonyl)imide (Li-TFSI) solution (170 mg Li-TFSI in 1 mL acetonitrile, Sigma-Aldrich)), and 8.2  $\mu\text{L}$  of 4-tertbutylpyridine (TBP) all dissolved in 1 mL of chlorobenzene (Sigma-Aldrich) are spin coated on top of the perovskite at 2500 rpm and 2500 rpm s $^{-1}$  for 45 s. The devices are finished by evaporating 50 nm of Au through a metal mask under high vacuum ( $< 3 \times 10^{-4}$  Pa). The solar cell area is equal to 0.15 cm $^2$ .

For NIR-transparent flexible PSCs, an ~20-nm-thick  $\text{MoO}_x$  layer is deposited on top of the Spiro-OMeTAD via thermal evaporation ( $< 3 \times 10^{-4}$  Pa), which is then covered by ~200 nm of IZO as the transparent electrode (200 W). Ni/Al grids with a 50 nm/4000 nm thickness are deposited by e-beam evaporation. The solar cell area is defined by mechanical scribing.

## Characterization

The current density-voltage characteristics of PSCs are measured under standard simulated AM1.5 G illumination using a Keithley 2400 source meter. The illumination intensity is calibrated to 1000 W m $^{-2}$  using a certified single-crystalline silicon solar cell. The *J*–*V* measurement is performed in both the forward (from –0.1 to 1.4 V) and backward (from 1.4 to –0.1 V) direction separately without any pretreatment (e.g., light soaking, holding at forward bias for a certain time, etc.). The scan rate and delay time are 0.3 V s $^{-1}$  and 10 ms, respectively. The external quantum efficiency is measured with a lock-in amplifier. The probing beam is generated by a chopped white source (900 W, halogen lamp, 260 Hz) and a dual-grating

monochromator. The beam size is adjusted to ensure that the illumination area is fully inside the cell area. A certified single-crystalline silicon solar cell is used as the reference cell. White light bias is applied during the measurement with ~0.1 sun intensity. The steady-state efficiency as a function of time is recorded using a maximum power point tracker, which adjusts the applied voltage to reach the maximum power point (perturb and observe algorithm). The starting voltage is set to be 0.1 V. The tandem device in the four-terminal configuration is characterized as reported elsewhere<sup>12</sup>.

The bending tests are carried out using metallic cylinders to define the curvature radius. Cylinders with a diameter of 12 mm and 8 mm are used for bending with radii of 6 mm and 4 mm, respectively. The devices are bent repeatedly on these cylinders.

X-ray diffraction patterns were obtained in the Bragg-Brentano geometry by using a X'Pert PRO  $\theta$ – $2\theta$  scan ( $\text{Cu-K}_{\alpha 1}$  radiation,  $\lambda = 1.5406 \text{ \AA}$ ) from 10 to 60° ( $2\theta$ ) with a step interval of 0.0167°.

The SEM images of the samples were investigated with a Hitachi using a voltage and current of 5 kV and 10 mA, respectively. A thin layer of Pt (1 nm) was coated on top of the sample to avoid the charging effect.

The morphology images were acquired using an AFM Bruker ICON operated in PeakForce QNM mode (based on PeakForce Tapping technology).

Reflectance and transmittance were measured using a UV-3600 Shimadzu UV-VIS-NIR spectrophotometer equipped with an integrating sphere. Ellipsometry measurements were carried out with a Woollam M2000 V-NIR instrument in a wavelength range of 370–1670 nm at incidence angles of 50°, 60° and 70°. The refractive indices of the different layers were determined by processing of reflectance, transmittance and ellipsometry data using the ReFFit software<sup>21</sup>. The dielectric functions were constructed as the sums of Lorentz and Tauc-Lorentz oscillators, ensuring consistency with the Kramers-Kroning relations. The optical propagation in the solar cell was simulated using the transfer matrix method (TMM) implemented in the tmm python package<sup>22</sup>.

## Results and discussion

The flexible substrate used in this work is commonly applied as an encapsulation front sheet for flexible CIGS solar modules, and it displays ultralow optical absorptance and water vapor transmission rate, as reported previously<sup>8</sup>. The use of this particular substrate opens up the way to the direct integration of a flexible perovskite top cell in a traditional flexible CIGS module manufacturing line. Supplementary Figure S1a shows the optical properties of the flexible substrate coated with an indium zinc oxide (IZO) transparent conductive oxide (TCO) layer. The average absorptance of the flexible substrate/TCO

layer stack is ~5% between 400 and 1000 nm. The IZO deposited by rf-magnetron sputtering shows a carrier mobility of  $54.8 \text{ cm}^2 \text{ V}^{-1} \text{ s}^{-1}$ , as determined by Hall measurements. As shown in Supplementary Figure S1b, from XRD analysis, the TCO layer is found to be amorphous, in accordance with other studies<sup>23</sup>.

A combination of spin-coated poly(ethylenimine) ethoxilated (PEIE) and thermally evaporated C<sub>60</sub> is used to enhance charge extraction and collection from the absorber to the anode<sup>24</sup>.

The perovskite absorber is deposited using a two-step hybrid vacuum-solution deposition process<sup>12</sup>. PbI<sub>2</sub> is thermally evaporated and converted to CH<sub>3</sub>NH<sub>3</sub>PbI<sub>3</sub> by spin coating CH<sub>3</sub>NH<sub>3</sub>I (MAI) in 2-propanol solution. Supplementary Figure S2a shows a cross-sectional SEM image of the flexible PSC using a two-step hybrid process. As shown in Supplementary Figure S2b, we are able to demonstrate a flexible PSC, which shows an open-circuit voltage ( $V_{oc}$ ) of 1.07 V, a short-circuit current ( $J_{sc}$ ) of 18.5 mA cm<sup>-2</sup> and a fill factor (FF) of 72.9% under forward measurement while also showing a  $V_{oc}$  of 1.05 V,  $J_{sc}$  of 18.3 mA cm<sup>-2</sup> and FF of 72.1% under backward measurement. The cell is tested at the maximum power point (MPP) under continuous illumination to evaluate the efficiency under operating conditions. The device shows a power conversion efficiency of 14.2% (Supplementary Figure S2c). Supplementary Figure S2d shows the external quantum efficiency (EQE) of the device, with the integrated  $J_{sc}$  value for AM1.5 G determined to be 18.5 mA cm<sup>-2</sup>.

Our samples contain residual PbI<sub>2</sub> (Supplementary Figure S2e, ~12.7%), which has been confirmed to be beneficial for suppressing non radiative recombination<sup>25</sup>.

In comparison to state-of-the-art of flexible PSCs<sup>6</sup>, the main bottleneck in our device is represented by the low  $J_{sc}$  values. One of the main causes for the low current yield is related to the limited absorption of the thin perovskite layer (<300 nm) deposited in the two-step hybrid process (Supplementary Figure S2a). A straightforward solution would be to simply increase the perovskite absorber thickness by deposition of a thicker PbI<sub>2</sub> layer.

As reported by other studies, for a two-step deposition method, increasing the thickness of the perovskite absorber does not result in direct efficiency improvement<sup>26-28</sup>. Having a thick and compact PbI<sub>2</sub> layer hinders efficient diffusion and intercalation of organic cations. By increasing the thickness of the lead iodide, higher charge transport resistance and stronger charge recombination have been observed<sup>27</sup>.

We increased the PbI<sub>2</sub> thickness to 200 nm to eventually obtain a thicker perovskite layer. Different MAI concentrations were investigated: 70, 75 and 80 mg mL<sup>-1</sup> (Supplementary Figure S3). Our results show that an increase in the inorganic layer thickness does not result in

efficiency improvements with respect to optimum thinner absorber thicknesses (Supplementary Figure S2). As the organic precursor concentration is increased,  $J_{sc}$  increases, saturating at higher concentrations, in contrast with an observed decrease in FF values. A too low MAI concentration results in limited conversion to the perovskite phase. On the other hand, a certain amount of unreacted lead iodide has been confirmed to be beneficial for device performance<sup>25,29</sup>. For this reason, a too large amount of MAI must be avoided, considering the detrimental effects observed due to an excess of uncoordinated MA<sup>+</sup> ions<sup>30</sup>.

To effectively increase the absorber thickness, and consequently the device efficiency, we believe that the MAI intercalation needs to be facilitated by appropriate tailoring of the PbI<sub>2</sub> morphology. Figure 1 shows a schematic for the proposed multistage deposition protocol. Thermally evaporated PbI<sub>2</sub> on top of amorphous C<sub>60</sub> grows in a compact morphology with a root mean square (RMS) roughness of ~9 nm as measured by AFM. The isotropic nature of the substrate and interface surface energy favors a preferential growth parallel to the substrate<sup>20</sup>. Once the organic precursor is deposited and the film is annealed, a compact perovskite layer forms with a surface RMS roughness of ~22 nm. The proposed modified process relies on the vacuum deposition of PbI<sub>2</sub> on top of the perovskite. The absorber displays a crystalline surface. The anisotropy of both the substrate and interface surface energy dictates the formation of a noncompact nanoplate-like PbI<sub>2</sub> morphology<sup>20</sup>. This open framework will facilitate efficient organo-halide diffusion and intercalation in the following spin coating step. The nanoplate-like morphology is verified by SEM, with the RMS roughness of the inorganic layer deposited on top of the perovskite found to be ~28 nm. Eventually, the organic precursor is deposited by spin coating. The absorber layer obtained via the multistage process shows a compact morphology without a clear separation between the two deposition stages. The RMS roughness of the final perovskite absorber is found to be equal to ~37 nm.

As there is an optimum proportion between the compact PbI<sub>2</sub> layer thickness and organic cation concentration, an optimum ratio has to be defined for the nanoplate-like PbI<sub>2</sub> layer thickness as well. It is necessary to provide an appropriate concentration of organic cations for a given inorganic layer thickness. This concentration must be sufficient to break the weak Van der Waals forces between the layers of PbI<sub>2</sub> and convert them into PbI<sub>6</sub> octahedral networks. Meanwhile, the concentration should not be too high to avoid steric hindrance and an excess of unreacted organic moieties.

Different combinations of second-stage nanoplate-like PbI<sub>2</sub> layer thicknesses and MAI concentrations were investigated and compared. Supplementary Figure S4a shows multistage deposition with 80 nm of PbI<sub>2</sub> as the

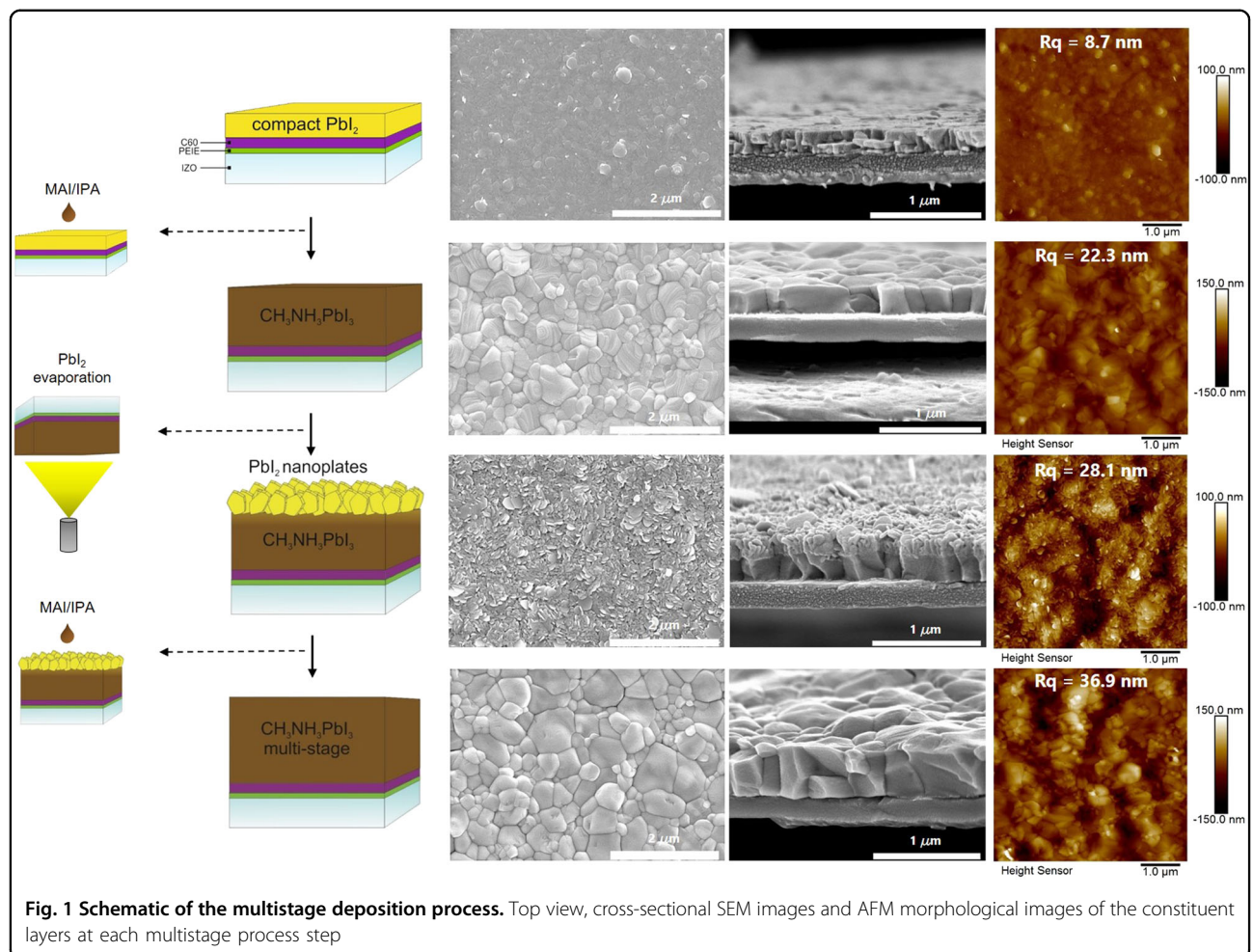


**Fig. 1 Schematic of the multistage deposition process.** Top view, cross-sectional SEM images and AFM morphological images of the constituent layers at each multistage process step

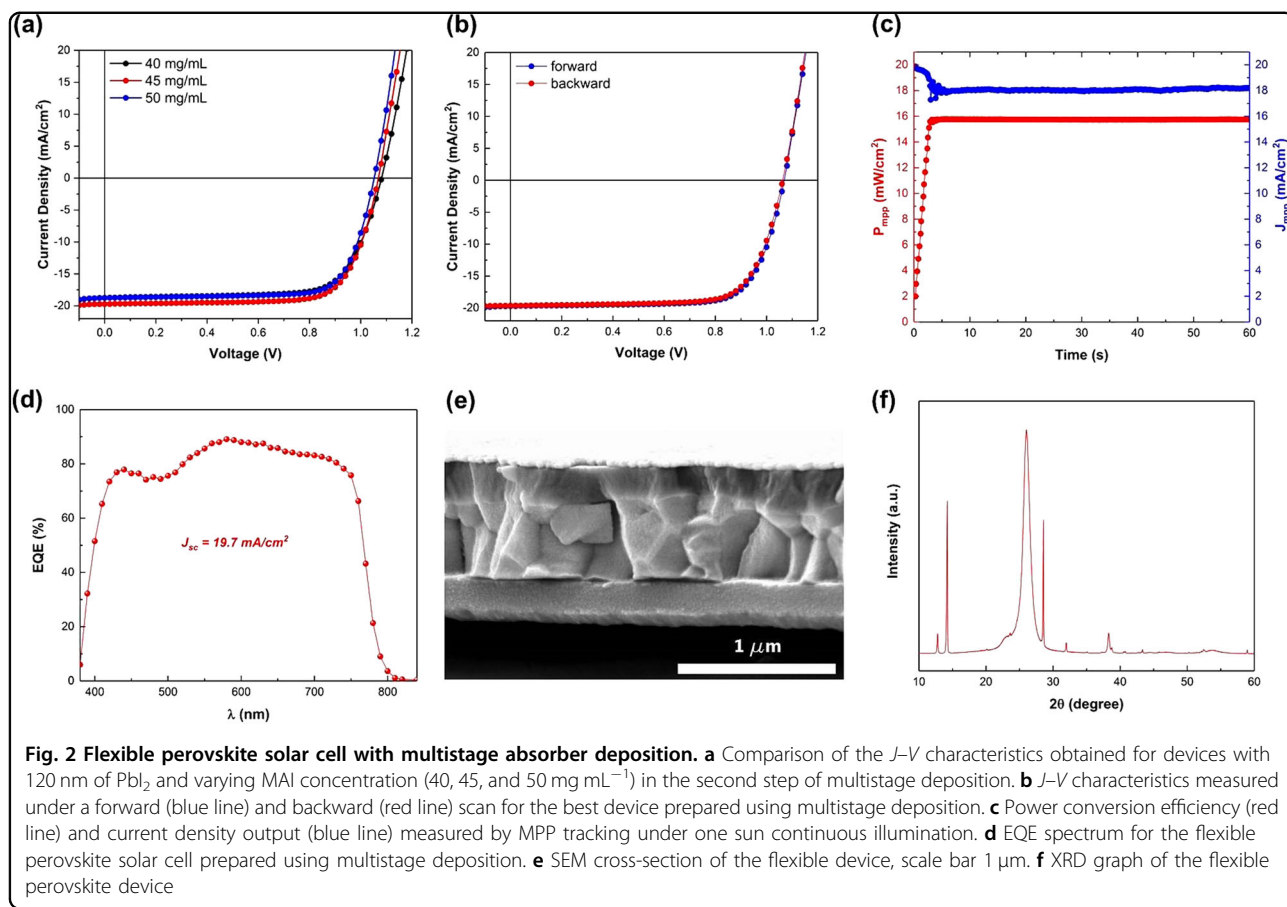
second step. The MAI concentration was changed from 20 to 30 mg mL<sup>-1</sup>, with an efficiency of 15.3% (under MPP tracking) obtained for a concentration of 25 mg mL<sup>-1</sup>. Supplementary Figure S4b presents the device performance with 100 nm of  $\text{PbI}_2$  and MAI concentrations that vary from 30 to 40 mg mL<sup>-1</sup>: 35 mg mL<sup>-1</sup> of MAI leads to an efficiency of 15.4%. Supplementary Figure S4c shows deposition with 140 nm of  $\text{PbI}_2$  and MAI concentrations varying from 45 to 55 mg mL<sup>-1</sup>, with the best efficiency of 14.7% reached at 50 mg mL<sup>-1</sup>. The very thick absorber results in poorer device performance due to limited carrier diffusion length in the pure  $\text{MAPI}_3$  perovskite<sup>31</sup>.

The optimum proportion is achieved with a 120-nm-thick of nanoplate-like  $\text{PbI}_2$  layer (Fig. 2a) and with 45 mg mL<sup>-1</sup> of MAI in the second stage (Fig. 2b). We are able to demonstrate a flexible PSC with a steady-state efficiency of 15.8% (Fig. 2c). The device shows a  $V_{oc}$  of 1.07 V,  $J_{sc}$  of 19.7 mA cm<sup>-2</sup> and an FF of 74.0% when measured in the forward direction and a  $V_{oc}$  of 1.06 V,  $J_{sc}$  of 19.6 mA cm<sup>-2</sup> and an FF of 73.4% when measured in the backward direction. As can be observed from the EQE measurements (Fig. 2d), a significant improvement with respect to

the two-step hybrid process is achieved at long wavelengths, indicating stronger absorption in the perovskite layer. The final device displays a compact absorber layer that contains residual  $\text{PbI}_2$  (Fig. 2e, f).

From an application point of view, mechanical resistance against bending is pivotal to ensure working flexible photovoltaic devices. The bottleneck of flexibility dwells in the brittle TCO, which is usually crystalline ITO<sup>32</sup>. It is observed that when crystalline ITO is used as the TCO, flexible PSC performance decreases well below 60% of the initial value after 1000 cycles at a bending radius of 4 mm<sup>33</sup>. Different strategies have been proposed to overcome this problem. Among them, amorphous TCO films deposited at low temperature have been used to enhance flexibility in organic photovoltaics. It has been shown that amorphous films have a robust structure against external dynamic stresses compared with crystalline films<sup>34,35</sup>.

In our flexible perovskite device structure, we employ ~200 nm of amorphous IZO as the TCO. To demonstrate mechanical stability against bending, we tested cells at bending radii of 6 mm and 4 mm for 1000 bending cycles.

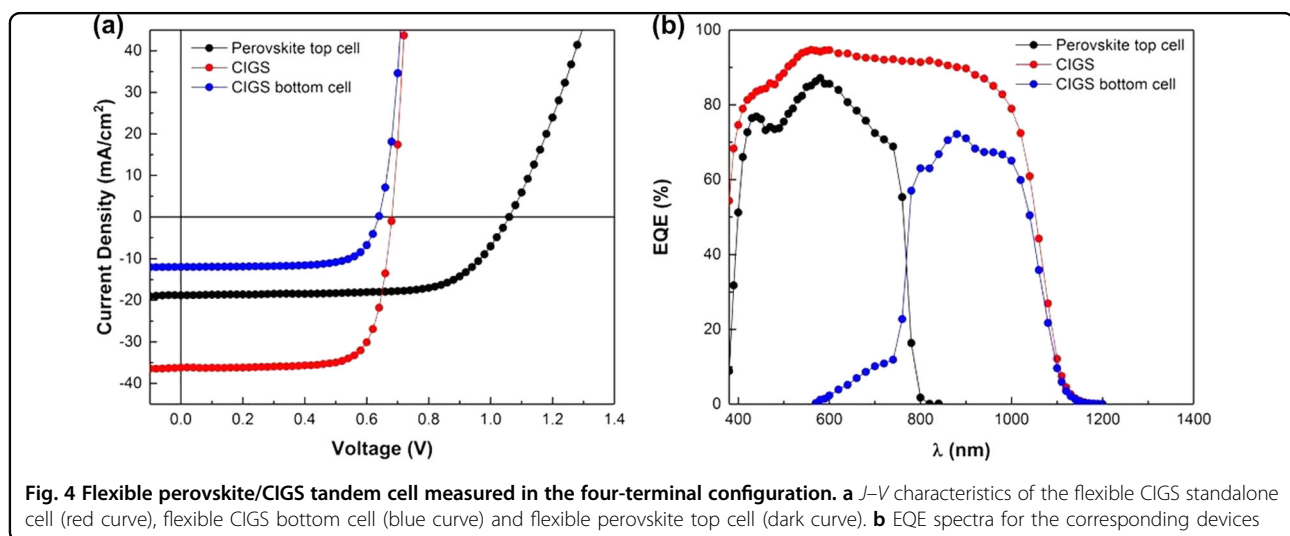
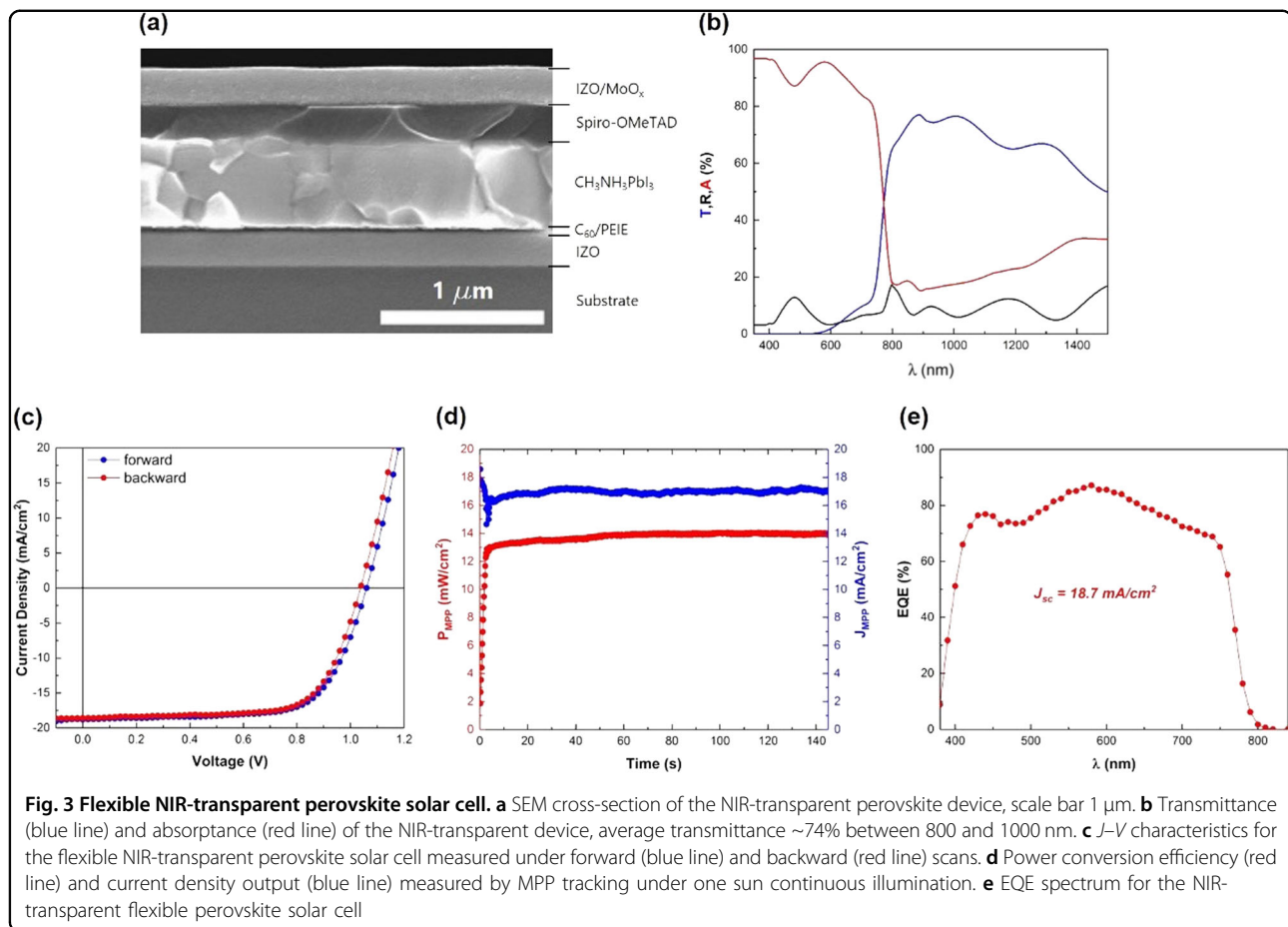


Supplementary Figure S5a shows stability against a bending radius of 6 mm. The device displays an efficiency at 1000 bending cycles that is ~90% of the initial power conversion efficiency. Stability test against a bending radius of 4 mm is presented in Supplementary Figure S5b. The device retains more than 80% of the original efficiency at 1000 bending cycles. These bending performances exceed those consistently obtained in the literature using crystalline ITO as the TCO<sup>32,33</sup>. The achievable robustness to bending is controlled by a complex interplay among defects, residual film stresses, cohesive properties, and so forth. Furthermore, the suppression of crystallization is required to obtain a stress-free or reduced-stress film<sup>34,36</sup>.

For application in four-terminal tandem devices, the top cell requires a near-infrared (NIR) transparent back electrode to guarantee that low-energy photons can reach the bottom cell. For the transparent electrode, a combination of  $\text{MoO}_x$  and IZO was used. Figure 3a shows the SEM cross-section of the NIR-transparent flexible PSC using multistage deposition. The cell displays an average transmittance of ~74% between 800 and 1000 nm (Fig. 3b). The device shows a  $V_{\text{oc}}$  of 1.06 V,  $J_{\text{sc}}$  of 18.7  $\text{mA cm}^{-2}$  and an FF of 69.0% when measured in forward direction and a

$V_{\text{oc}}$  of 1.04 V,  $J_{\text{sc}}$  of 18.6  $\text{mA cm}^{-2}$  and an FF of 69.4% when measured in the backward direction (Fig. 3c). The NIR-transparent solar cell reaches an efficiency of 14.0% at the MPP under one-sun illumination (Fig. 3d). The integrated  $J_{\text{sc}}$  value determined from EQE (Fig. 3e) is 18.7  $\text{mA cm}^{-2}$ . We demonstrate a perovskite/CIGS tandem device in the four-terminal configuration, where the top and bottom cells are grown on flexible substrates. Figure 4a, b displays the  $J$ - $V$  curves and EQE spectra for the top PSC, CIGS standalone cell and CIGS bottom cell. Table 1 summarizes the photovoltaic parameters of the corresponding devices. The flexible perovskite/CIGS tandem device measured in four-terminal configuration shows an efficiency of 19.6%, starting from an 18.9% flexible CIGS solar cell.

It is clear that increasing the absorption of the top cell results in a lower bottom cell current yield, which could limit the final tandem device performance. For this reason, we decided to compare the multistage perovskite deposition with two-step hybrid deposition for top cell application. The  $J$ - $V$  characteristics of the latter NIR-transparent flexible PSC show a  $V_{\text{oc}}$  of 1.10 V,  $J_{\text{sc}}$  of 17.5  $\text{mA cm}^{-2}$  and FF of 68.1% under the forward scan and a  $V_{\text{oc}}$  of 1.08 V,  $J_{\text{sc}}$  of 17.4  $\text{mA cm}^{-2}$  and FF of 68.9% when measured under the



backward scan (Supplementary Figure S6a). The device displays a steady-state efficiency of 13.1% (Supplementary Figure S6b). The NIR-transparent device, developed by the two-step hybrid process, shows a lower current yield with respect to multistage deposition. The reason for this is due

to the lower absorption in the long wavelength region of the EQE (Supplementary Figure S6c). Combining the perovskite top cell with the flexible CIGS bottom cell (Supplementary Table S1), an efficiency of 19.2% is achieved (Supplementary Figure S6d, e). Although the bottom cell

**Table 1** J-V parameters for each constituent solar cell in the tandem device

Solar cell	$V_{oc}$ (V)	$J_{scv}$ ( $\text{mA cm}^{-2}$ )	FF (%)	$\eta$ (%)	$\eta_{MPP}$ (%)	Area ( $\text{cm}^2$ )
Flexible CIGS	0.69	36.3	75.4	18.9	18.9	0.213
Flexible CIGS bottom cell	0.65	12.0	71.6	5.6	5.6	0.213
Flexible perovskite top cell	1.06	18.7	68.9	13.7	14.0	0.27
Flexible perovskite/CIGS four-terminal tandem configuration					19.6	

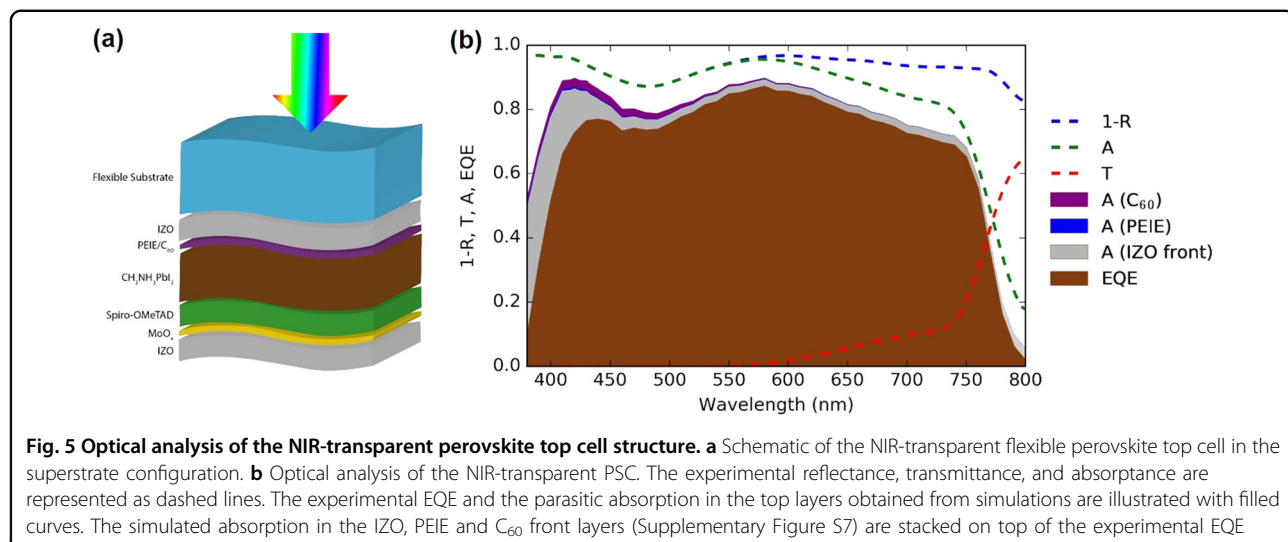
efficiency is greater (due to the higher absorption in the CIGS), the tandem device with a multistage top cell still outperforms the device developed using the two-step hybrid process due to the higher performance of the top cell.

To assess potential pathways to further improve flexible perovskite/CIGS tandem solar cells, we carried out optical analysis of the NIR-transparent perovskite top cell structure as an example of a low-temperature *n-i-p* PSC that can be deposited on flexible substrates (Fig. 5a). The transfer matrix method (TMM) was used to simulate the reflectance, transmittance of the multilayer structure and the absorption spectra of the different layers. The layers were considered optically flat (no interface roughness was taken into account). Complex refractive indices were either characterized in house (IZO front and rear TCO, PEIE,  $C_{60}$  and  $\text{MoO}_x$ ) or taken from the literature ( $\text{MAPbI}_3$  and Spiro-OMeTAD)<sup>37</sup>. Supplementary Figure S7 presents experimental data and best fits to the transmittance, reflectance and ellipsometry spectra of the layers used for the determination of the refractive indices. Supplementary Figure S8 displays experimental and TMM-based simulations of the reflectance, transmittance and absorptance of the NIR-transparent perovskite top cell in the visible range, with the layer thicknesses reported in Supplementary Table S2. The discrepancies between experimental and simulated reflectance (and absorptance) are related to light scattering and to the different substrates considered in the simulations with respect to the actual substrate (notably, including the encapsulation front sheet with specific oxide coatings). The optical losses in each of the layers can be evaluated in terms of the corresponding losses in the short-circuit current (Table S2) using AM1.5 G irradiance. As shown in Fig. 5b, the presence of the IZO front TCO and the ETL (PEIE interlayer and  $C_{60}$ ) leads to the absorption of light that cannot reach the perovskite absorber. The corresponding  $J_{sc}$  losses in the front TCO and ETL amount to 1.0 and  $0.2 \text{ mA cm}^{-2}$ , respectively. This loss due to parasitic absorption can be mitigated by using an improved front TCO with comparatively lower absorption (our IZO presents non-negligible absorption in the visible) and by the use of a more transparent low-temperature ETL (as inorganic ones). Reflection losses can be observed especially between 450–500 nm, which can be reduced by an appropriate

anti-reflection (AR) coating, such as a transparent layer with a refractive index intermediate between that of air and the substrate and/or the substrate and the front TCO. At longer wavelengths, reflectance can be reduced by using an AR coating at the rear TCO/air interface. For  $\lambda > 600 \text{ nm}$ , the NIR-transparent solar cell presents transmission losses due to the absence of an internal back reflector typical of opaque devices (metal back contact). In this region (600–800 nm), the effect on the transmittance of the layers deposited after  $\text{MAPbI}_3$  is negligible, such that the photons lost in this wavelength range are efficiently absorbed by the bottom cell, as shown in Fig. 4b. Lastly, hints to the collection and recombination losses are obtained by combining the experimental and simulation data, as described by Armin et al.<sup>38</sup>. In the case of our NIR-transparent cell, the sum of the experimental EQE with the predicted parasitic absorption in the front layers does not quite reach the level of the experimental absorptance of the device, as shown in Fig. 5b. This difference is seemingly independent from the excitation wavelength and is tentatively ascribed to collection losses and/or to recombination. We believe that these losses can be mitigated by proper interface engineering and by processing of higher-quality perovskite absorbers.

## Conclusion

We have demonstrated a modified hybrid vacuum-solution deposition method to tailor  $\text{PbI}_2$  growth for effectively increasing the perovskite thickness. Through multistage deposition, an improvement in performance for flexible PSCs, from a steady-state efficiency of 14.2 to 15.8%, was shown. Using an amorphous TCO (IZO), we were able to demonstrate superior bending stability with respect to the traditional crystalline TCO used for flexible PSCs. Flexible devices retained 90 and 80% of the initial efficiency after 1000 bending cycles at bending radii of 6 and 4 mm, respectively. We have developed a flexible NIR-transparent PSC with a steady-state efficiency of 14.0%. The devices were grown onto a flexible foil, which is used as an encapsulation front sheet for CIGS solar modules. By combining the flexible perovskite top cell with a flexible CIGS bottom cell, a flexible perovskite/CIGS tandem cell, with an efficiency of 19.6% measured in the four-terminal configuration, was demonstrated.



Through analyses of the optical losses and TMM-based simulations, we identified the next steps towards realizing higher efficiency NIR-transparent flexible PSCs.

In this work, we described a method to engineer the  $PbI_2$  layer morphology using vacuum deposition. The multistage deposition protocol widens the potential for use of the hybrid vacuum-solution process towards the realization of highly efficient devices by precise morphological tuning.

#### Acknowledgements

This work was financial funded by the Swiss National Science Foundation (SNF)-NRP70, PV2050 (project NO: 407040\_153976 and 407040\_153916), SNF-NanoTera and Swiss Federal Office of Energy (SYNERGY: 20NA21\_150950), NanoTera (project Synergy Gateway) and FP7 APPOLO project (609355). We acknowledge the access to the Scanning Probe Microscopy User Lab at Empa for the (AFM) measurements. A special thank you goes to Marc Padrutt, a visiting student in our group.

#### Conflict of interest

The authors declare that they have no conflict of interest.

#### Publisher's note

Springer Nature remains neutral with regard to jurisdictional claims in published maps and institutional affiliations.

**Supplementary information** is available for this paper at <https://doi.org/10.1038/s41427-018-0099-1>.

Received: 14 July 2018 Revised: 11 September 2018 Accepted: 1 October 2018.

Published online: 16 November 2018

#### References

- Green, M. A., Ho-Baillie, A. & Snaith, H. J. The emergence of perovskite solar cells. *Nat. Photonics* **8**, 506 (2014).
- De Wolf, S. et al. Organometallic halide perovskites: sharp optical absorption edge and its relation to photovoltaic performance. *J. Phys. Chem. Lett.* **5**, 1035–1039 (2014).
- Werner, J., Niesen, B. & Ballif, C. Perovskite/silicon tandem solar cells: marriage of convenience or true love story? – an overview. *Adv. Mater. Interfaces* **5**, 1700731 (2018).
- Eperon, G. E., Hörantner, M. T. & Snaith, H. J. Metal halide perovskite tandem and multiple-junction photovoltaics. *Nat. Rev. Chem.* **1**, 0095 (2017).
- Shen, H. et al. Mechanically-stacked perovskite/CIGS tandem solar cells with efficiency of 23.9% and reduced oxygen sensitivity. *Energy Environ. Sci.* **11**, 394–406 (2018).
- Bi, C., Chen, B., Wei, H., DeLuca, S. & Huang, J. Efficient flexible solar cell based on composition-tailored hybrid perovskite. *Adv. Mater.* **29**, 1605900 (2016).
- Chirilă, A. et al. Potassium-induced surface modification of Cu(In,Ga)Se<sub>2</sub> thin films for high-efficiency solar cells. *Nat. Mater.* **12**, 1107–1111 (2013).
- Pisoni, S. et al. Flexible NIR-transparent perovskite solar cells for all-thin-film tandem photovoltaic devices. *J. Mater. Chem. A* **5**, 13639–13647 (2017).
- Jung, H. S. & Park, N.-G. Perovskite solar cells: from materials to devices. *Small* **11**, 10–25 (2015).
- Momblona, C. et al. Efficient vacuum deposited p-i-n and n-i-p perovskite solar cells employing doped charge transport layers. *Energy Environ. Sci.* **9**, 3456–3463 (2016).
- Ávila, J., Momblona, C., Boix, P. P., Sessolo, M. & Bolink, H. J. Vapor-deposited perovskites: the route to high-performance solar cell production? *Joule* **1**, 431–442 (2017).
- Fu, F. et al. Low-temperature-processed efficient semi-transparent planar perovskite solar cells for bifacial and tandem applications. *Nat. Commun.* **6**, 8932 (2015).
- Yang, W. S. et al. Iodide management in formamidinium-lead-halide-based perovskite layers for efficient solar cells. *Science* **356**, 1376–1379 (2017).
- Wojciechowski, K. et al.  $C_{60}$  as an efficient n-type compact layer in perovskite solar cells. *J. Phys. Chem. Lett.* **6**, 2399–2405 (2015).
- Ahmad, S., Kanaujia, P. K., Niu, W., Baumberg, J. J. & Vijaya Prakash, G. In situ intercalation dynamics in inorganic–organic layered perovskite thin films. *ACS Appl. Mater. Interfaces* **6**, 10238–10247 (2014).
- Mitzi, D. B. in *Progression in Inorganic Chemistry* (ed Mitzi, D. B.) 1–121 (Wiley-Blackwell, 2007), Canada.
- Wu, Y. et al. Retarding the crystallization of  $PbI_2$  for highly reproducible planar-structured perovskite solar cells via sequential deposition. *Energy Environ. Sci.* **7**, 2934–2938 (2014).
- Tu, Y. et al. Solvent engineering for forming stonehenge-like  $PbI_2$  nanostructures towards efficient perovskite solar cells. *J. Mater. Chem. A* **5**, 4376–4383 (2017).
- Zhang, T., Yang, M., Zhao, Y. & Zhu, K. Controllable sequential deposition of planar  $CH_3NH_3PbI_3$  perovskite films via adjustable volume expansion. *Nano Lett.* **15**, 3959–3963 (2015).
- Fu, F. et al. Controlled growth of  $PbI_2$  nanoplates for rapid preparation of  $CH_3NH_3PbI_3$  in planar perovskite solar cells. *Phys. Status Solidi A* **212**, 2708–2717 (2015).

21. RefITprogram. <https://sites.google.com/site/refitprogram/home>.
22. Byrnes, S. J. Multilayer optical calculations. *arXiv*. <http://arxiv.org/abs/1603.02720> (2016).
23. Morales-Masis, M., Nicolas, S. M. D., Holovsky, J., Wolf, S. D. & Ballif, C. Low-temperature high-mobility amorphous IZO for silicon heterojunction solar cells. *IEEE J. Photovolt.* **5**, 1340–1347 (2015).
24. Pisoni, S. et al. Impact of interlayer application on band bending for improved electron extraction for efficient flexible perovskite mini-modules. *Nano Energy* **49**, 300–307 (2018).
25. Bi, D. et al. Efficient luminescent solar cells based on tailored mixed-cation perovskites. *Sci. Adv.* **2**, e1501170 (2016).
26. Xiao, Z. et al. Efficient, high yield perovskite photovoltaic devices grown by interdiffusion of solution-processed precursor stacking layers. *Energy Environ. Sci.* **7**, 2619–2623 (2014).
27. Liu, D., Gangishetty, M. & L. Kelly, T. Effect of CH<sub>3</sub>NH<sub>3</sub>PbI<sub>3</sub> thickness on device efficiency in planar heterojunction perovskite solar cells. *J. Mater. Chem. A* **2**, 19873–19881 (2014).
28. Liu, D. et al. Tailoring morphology and thickness of perovskite layer for flexible perovskite solar cells on plastics: the role of CH<sub>3</sub>NH<sub>3</sub>I concentration. *Sol. Energy* **147**, 222–227 (2017).
29. Cao, D. H. et al. Remnant PbI<sub>2</sub>, an unforeseen necessity in high-efficiency hybrid perovskite-based solar cells? *APL Mater.* **2**, 091101 (2014).
30. Cheng, Y. et al. Spectroscopic study on the impact of methylammonium iodide loading time on the electronic properties in perovskite thin films. *J. Mater. Chem. A* **4**, 561–567 (2016).
31. Stranks, S. D. et al. Electron-hole diffusion lengths exceeding 1 micrometer in an organometal trihalide perovskite absorber. *Science* **342**, 341–344 (2013).
32. Poorkazem, K., Liu, D. & L. Kelly, T. Fatigue resistance of a flexible, efficient, and metal oxide-free perovskite solar cell. *J. Mater. Chem. A* **3**, 9241–9248 (2015).
33. Wang, Y. et al. High-efficiency flexible solar cells based on organometal halide perovskites. *Adv. Mater.* **28**, 4532–4540 (2016).
34. Lee, H.-M., Kang, S.-B., Chung, K.-B. & Kim, H.-K. Transparent and flexible amorphous In-Si-O films for flexible organic solar cells. *Appl. Phys. Lett.* **102**, 021914 (2013).
35. Morales-Masis, M., Wolf, S. D., Woods-Robinson, R., Ager, J. W. & Ballif, C. Transparent electrodes for efficient optoelectronics. *Adv. Electron. Mater.* **3**, 1600529 (2017).
36. Heo, G.-S., Gim, I.-G., Lee, H.-K., Song, J.-H. & Kim, T.-W. Investigation of bending stability of amorphous Zn-In-Sn-O thin films on flexible poly(ether sulfone) substrates. *Jpn. J. Appl. Phys.* **49**, 031104 (2010).
37. Eerden, Mvan et al. Optical analysis of planar multicrystalline perovskite solar cells. *Adv. Opt. Mater.* **5**, 1700151 (2017).
38. Armin, A. et al. Quantum efficiency of organic solar cells: electro-optical cavity considerations. *ACS Photonics* **1**, 173–181 (2014).